Light absorption enhancement in ultrathin perovskite solar cells using light scattering of high-index dielectric nanospheres

HYEONWOO KIM,[1] HOJAE KWAK,[1] INCHEOL JUNG,[1] MI SUK KIM,[1] JEONGHYUN KIM,[2,4] HUI JOON PARK,[3,5] AND KYU-TAE LEE[1,6] (iD)

[1]*Department of Physics, Inha University, Incheon 22212, Republic of Korea*
[2]*Department of Electronic Convergence Engineering, Kwangwoon University, Seoul 01897, Republic of Korea*
[3]*Department of Organic and Nano Engineering, Hanyang University, Seoul 04763, Republic of Korea*
[4]*jkim@kw.ac.kr*
[5]*huijoon@hanyang.ac.kr*
[6]*ktlee@inha.ac.kr*

Abstract: Arrays of high-index dielectric nanoparticles supporting both electrical and magnetic resonances have gained increasing attention for their excellent light-trapping (LT) effects, thus greatly improving the performance of ultrathin solar cells. This work explores front-located, high-index dielectric subwavelength nanosphere arrays as an efficient and broadband LT structure patterned on top of an ultrathin perovskite solar cell (PSC) for a greatly enhanced absorption. Combined strong light scattering and anti-reflection properties achieved by optimized geometrical parameters of the LT structure lead to a broadband absorption enhancement in the ultrathin thickness of a photoactive layer (100 nm) yielding the short-circuit current density (J_{sc}) of 18.7 mA/cm^2, which is 31.7% higher than that of a planar counterpart. Moreover, effects of the LT structure on far-field radiation patterns, scattering cross-sections, multipoles' contributions, and asymmetry parameters along with the incidence angle and polarization dependence are investigated. The present strategy could be applied to diverse applications, such as other ultrathin or semitransparent solar cells, absorbers and photodetectors.

1. Introduction

Organic-inorganic hybrid perovskite semiconductors have gained significant amount of attention for their potential as an excellent light absorbing material in various research areas including solar cells, light-emitting diodes and photodetectors [1–8]. The perovskite materials feature promising optoelectronic properties such as large absorption coefficient and cross section, long charge carrier diffusion length, high carrier mobility and tunable band gaps [1,9–13]. Such compelling properties of the perovskite materials enable the efficiency of perovskite solar cells (PSCs) to rise rapidly from 3.8% in 2009 to 25.6% in 2021 [14,15]. Great effort is also being applied to develop semitransparent PSCs for building-integrated photovoltaics (BIPVs) and highly efficient tandem cells where the PSCs are integrated with the other solar cells [16–20]. Moreover, the PSCs can be fabricated by using low-temperature solution-processing methods, which can make them especially appealing for low-cost, lightweight and flexible PV devices, thereby potentially extending the range of possible applications, such as consumer-oriented portable and wearable electronics, solar-powered aerial vehicles, and biomedical monitoring [21–26].

To realize the aforementioned applications, reducing the thickness of an active region in the PSCs is essential for attaining high optical transparency in the semitransparent PSCs or high mechanical flexibility in the flexible and lightweight PSCs. However, the light absorption is generally proportional to the thickness of the photoactive layer so the cell efficiency is significantly

limited by the reduced film thickness. Therefore, it is necessary to increase an optical path length where light travels in the photoactive layer combined with light-trapping (LT) schemes and thus increase the optical absorption associated with the photocurrent. Moreover, exploiting the LT allows manufacturing costs to be reduced for a given photoactive region thickness and open circuit voltage (V_{oc}) to be improved since photogenerated charge carriers do not have to diffuse as far before the collection yielding reduced recombination losses. A variety of the LT approaches to enhance the performance of the PSCs have been demonstrated based on textured perovskite absorbers and substrates, graded-refractive-index materials, plasmonic nanoparticles, surface plasmon resonances in subwavelength gratings, dielectric nanospheres embedded into the mesoporous layer, and microlens and prism arrays [27–39]. However, it is challenging to create such structures, and also directly structuring the photoactive layer increases both a surface roughness and a defect density, which can significantly degrade the electrical performance of the PSCs.

In this work, we investigate an effect of the Mie scattering by front-sided arrays of nanospheres on the absorption in the photoactive layer of the ultrathin PSCs. The results exhibit that markedly enhanced absorptions over a broad wavelength range can be achieved when the subwavelength array of high-index dielectric nanospheres is conformally coated with a low-index dielectric layer with the optimized diameter, spacing and thickness, resulting in the short-circuit current density (J_{sc}) increased from 14.2 mA/cm^2 to 18.7 mA/cm^2 for the PSCs with the 100 nm-thick perovskite photoactive layer. Physically thin but optically thick PSCs are enabled by an optical path length increase in the ultrathin photoactive layer contributing to the improved J_{sc}, which is confirmed by studying absorption distributions in the structure, far-field radiation patterns, scattering cross-sections, multipole resonance contributions, and asymmetry parameters. Lastly, we study how incident angles and polarizations affect the J_{sc} of the ultrathin PSCs. The presented LT structure can serve as a good encapsulation layer and can also be patterned at the final stage of a device fabrication minimizing charge carrier recombination and thus a degradation of the electrical performance. The described structural configuration can be easily adopted to improve the absorption property in various applications, such as other thin-film solar cells, photodiodes, sensors, and absorbers.

2. Results and discussion

Figure 1(a) shows a schematic diagram of a conventional planar PSC structure that is constructed from a front indium tin oxide (ITO, 100 nm) electrode, a poly(3,4-ethylenedioxythiophene) polystyrene sulfonate (PEDOT:PSS, 40 nm) hole transport layer, an ultrathin methylammonium lead iodide ($CH_3NH_3PBI_3$) perovskite (PVSK, 100 nm) photoactive layer, a phenyl-C_{61}-butyric acid methyl ester (PCBM, 70 nm)/zinc oxide (ZnO, 50 nm) double electron transport layer, and an aluminum (Al, 100 nm) rear contact/mirror, which is a flat reference structure. Figure 1(b) depicts the schematic view of the conventional PSC structure integrated with the high-index dielectric nanosphere array (NSA) conformally coated with a thin low-index dielectric layer. The high-index dielectric NSA leads to the strong light scattering in the forward direction for an efficient LT effect without significant absorptions at visible frequencies, while the low-index conformal dielectric coating functions as an anti-reflection (AR) coating. Although metallic nanospheres can excite localized surface plasmon resonances that can remarkably boost the absorption efficiency in the photoactive layer, the absorption enhancement in the photoactive layer occurs in a narrow wavelength range and the absorption in the metallic nanospheres is not trivial particularly in the visible spectrum so the dielectric NSA is chosen for the LT in this study [40,41]. Titanium dioxide (TiO_2) is selected as a material of the high-index NSA for the high scattering efficiency and silicon dioxide (SiO_2) is chosen as the AR coating material. It is noted that the TiO_2 NSA of the proposed LT structure can be created by a self-assembly process of the

colloidal monolayer of the TiO_2 nanoparticles or patterned by a nanoimprint lithography, and the conformal SiO_2 layer can be deposited by using either sputtering or atomic layer deposition.
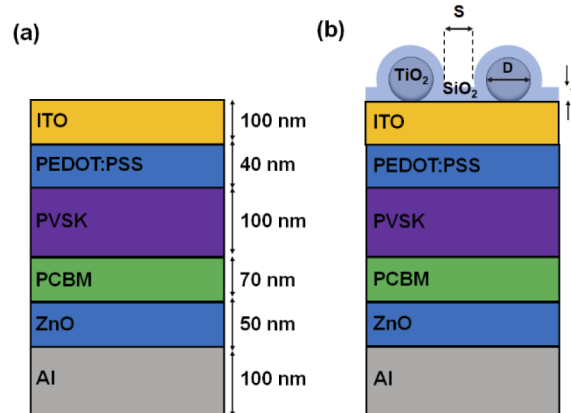

Fig. 1. Cross-sectional schematic diagrams of (a) a planar PSC structure and (b) the PSC structure incorporated with front-located TiO_2 NSA overlayed with a thin SiO_2 layer where the thickness of the PVSK photoactive layer is ultrathin (100 nm).

Three-dimensional (3D) simulations are carried out using the COMSOL Multiphysics software based on a finite element method to find the set of optimized geometrical parameters including a spacing (S), a diameter (D) of the TiO_2 nanospheres, and a thickness (t) of the conformal SiO_2 coating, which can contribute to the generation of the highest J_{sc} of the PSC structures with the ultrathin 100 nm-thick PVSK photoactive layer. The J_{sc} is regarded as a figure of merit to evaluate the performance of the LT effect from the TiO_2 NSA conformally coated with the SiO_2 AR coating (In the following, we refer to this LT structure as TiO_2/SiO_2 NSA).

Refractive index (n) and extinction coefficient (k) values for the PEDOT:PSS, PVSK, and PCBM, which are measured by using a spectroscopic ellipsometer (VASE, J. A. Woollam), are provided in Fig. 2, along with complex refractive indices of TiO_2, SiO_2, ITO, ZnO, and Al obtained from a website (https://refractiveindex.info).
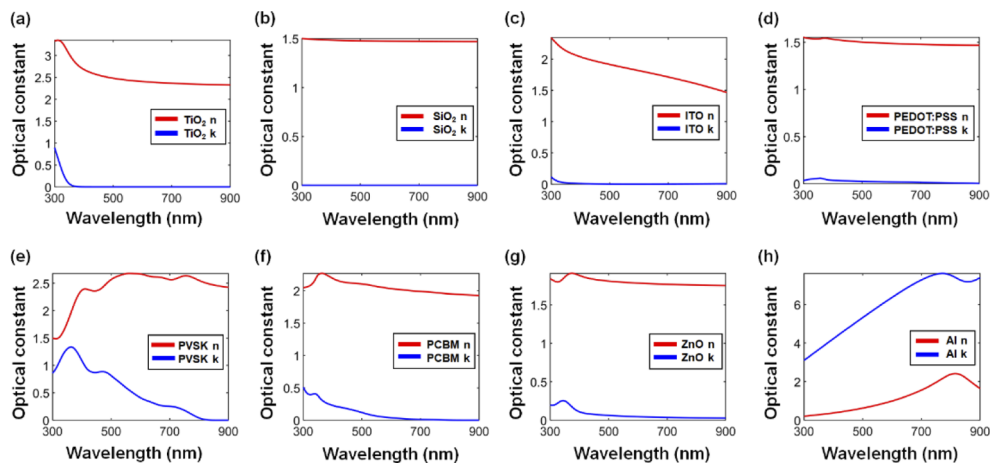

Fig. 2. Refractive index (n) and extinction coefficient (k) spectra of (a) TiO_2, (b) SiO_2, (c) ITO, (d) PEDOT:PSS, (e) PVSK, (f) PCBM, (g) ZnO, and (h) Al.

Geometrical parameters of the LT structure need to be optimized to achieve a maximum J_{sc}, which is done through a parameter sweep. In Figs. 3(a) – (d), calculated 2D contour plots of the J_{sc} as a function of S and D with thicknesses of the conformal SiO_2 coating of 0, 25, 50, and 75 nm are exhibited. By integrating the absorption spectrum in the PVSK photoactive layer, convoluted with the AM1.5 solar radiation spectrum, along the wavelength range from 300 nm to 900 nm, the J_{sc} can be calculated:

$$J_{SC} = \int_{300\,nm}^{900\,nm} \frac{e\lambda}{hc} QE(\lambda) I_{AM1.5}(\lambda) d\lambda \tag{1}$$

where e, λ, h, c, and $I_{AM1.5}(\lambda)$ are electron charge, wavelength, Plank constant, light velocity in free space, and solar power spectrum at AM1.5, respectively. An internal quantum efficiency is assumed to be equal to one, suggesting that the absorption spectrum in the photoactive layer directly corresponds to the quantum efficiency ($QE(\lambda)$). Maximum J_{sc} values of 16.5 mA/cm^2 with S of 280 nm and D of 240 nm, 17.7 mA/cm^2 with S of 240 nm and D of 220 nm, 18.5 mA/cm^2 with S of 200 nm and D of 220 nm, and 18.7 mA/cm^2 with S of 160 nm and D of 220 nm are achieved when t is equal to 0, 25, 50, 75 nm, respectively, implying that the maximum J_{sc} can be achieved when D is designed to be 220 nm regardless of t when applying the AR coating. It is noted that the J_{sc} value starts to decrease when t is greater than 75 nm from the calculation. Hence the optimized values of S of the TiO_2 NSA and t of the conformal SiO_2 coating can now be found by computing the J_{sc} with D of the TiO_2 nanospheres fixed at 220 nm, which is given in Fig. 4(a) presenting that the maximal J_{sc} value (18.7 mA/cm^2) can be attained from the LT structure with S of 160 nm, D of 220 nm, and t of 75 nm. In Fig. 4(b), simulated absorption spectra in the PVSK photoactive layer of the flat PSC structure (black), the PSC structure with the TiO_2 NSA (blue), and the PSC structure with the TiO_2/SiO_2 NSA (red) are depicted. For the flat PSC structure, two peaks in the absorption spectrum appear at 395 nm and 620 nm, which are attributed to the Fabry-Perot resonances.
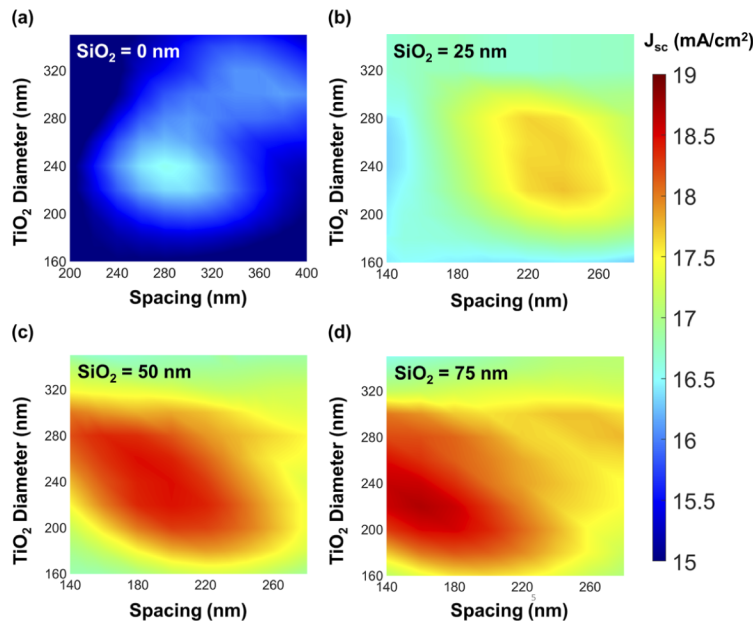

Fig. 3. Calculated 2D contour plots of the J_{sc} as a function of S of the TiO_2 NSA and D of the TiO_2 nanospheres with the conformal SiO_2 coating thickness of (a) 0 nm, (b) 25 nm, (c) 50 nm, and (d) 75 nm.
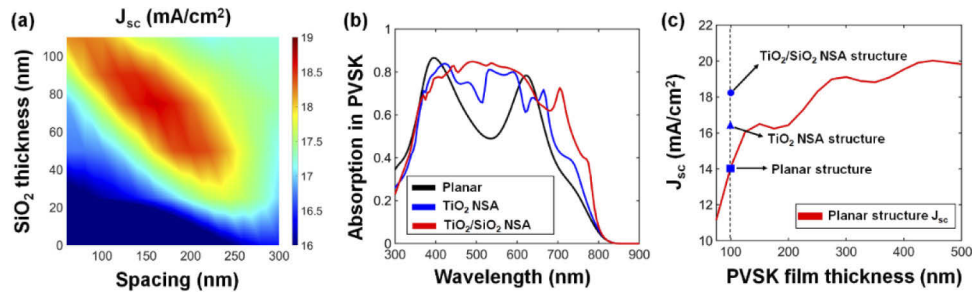
Fig. 4. (a) Calculated 2D contour plot of the J_{sc} as a function of S of the TiO$_2$ NSA and t of the conformal SiO$_2$ coating with D of the TiO$_2$ nanosphere fixed at 220 nm. (b) Simulated absorption spectra in the PVSK photoactive layer for the planar PSC structure (black) integrated with TiO$_2$ NSA (blue) and TiO$_2$/SiO$_2$ NSA (red). (c) Calculated J_{sc} values as a function of the thickness of the PVSK photoactive layer for the planar PSC structure along with the J_{sc} obtained from the flat PSC structure with the 100 nm-thick PVSK layer after the integration of the TiO$_2$ NSA (blue triangle) and TiO$_2$/SiO$_2$ NSA LT structures (blue circle).

The presence of the two peaks causes a deep valley in the absorption spectrum at 535 nm to occur between the two peaks, which significantly limits the performance of the PSC. By introducing the TiO$_2$ NSA into the planar PSC structure, the optical path length in the photoactive layer is prolonged by the light scattering in the forward direction yielding a broadband absorption enhancement between the two peaks with the slightly mitigated absorption at 395 nm and 620 nm, which is observed in a previous report [42]. The maximum J_{sc} of 16.5 mA/cm^2 is achieved from the TiO$_2$-NSA-integrated PSC structure at $S = 280$ nm and $D = 240$ nm without the conformal dielectric coating, with the improvement of 16.2% as compared with 14.2 mA/cm^2 attained from the planar PSC structure. Adding the conformal AR coating with the optimal thickness to the TiO$_2$-NSA-integrated PSC structure further improves the absorption in the PVSK photoactive layer over a broad wavelength range by reducing the reflection loss, thus achieving the J_{sc} of 18.7 mA/cm^2 corresponding to the enhancement of 31.7% compared to the planar PSC structure. Since the absorption of the TiO$_2$ NSA and the front ITO contact in the wavelengths shorter than 400 nm is high, there is a trivial contribution to the J_{sc} in this wavelength regime. It is important to note that such absorption losses in the shorter wavelength region can indeed be beneficial for achieving the stable PSCs yielding the longer lifetime, which is attributed to the fact that the performance of the PSCs is noticeably degraded by the constant ultraviolet illumination. Figure 4(c) exhibits the J_{sc} of the flat PSC structure as a function of the thickness of the PVSK photoactive layer. The J_{sc} of the TiO$_2$-NSA-integrated PSC structure with the 100 nm-thick PVSK layer is comparable to that of the flat PSC structure with the 200 nm-thick PVSK layer (16.4 mA/cm^2), and the J_{sc} of TiO$_2$/SiO$_2$-NSA-integrated PSC structure with the 100 nm-thick PVSK layer is found to be similar to that of the flat PSC structure with the 250 nm-thick PVSK layer (18.3 mA/cm^2). This implies that the thickness of the PVSK photoactive layer can be markedly reduced with the help of the LT effect by the integration of the TiO$_2$/SiO$_2$ NSA, which is greatly beneficial for the ultra-light and ultra-flexible or the semitransparent PSCs with high efficiency. Although we are mainly concerned with the optics rather than the electrical properties of the PSCs, the overall power conversion efficiency (PCE) can be roughly estimated by using 0.96 of V_{oc} and 0.757 of FF in a previous work yielding 13.59% of PCE [43].

To explore a better coupling of light into the PVSK photoactive layer by the TiO$_2$/SiO$_2$ NSA, the absorption profiles in each layer of the PSC structures without and with the TiO$_2$/SiO$_2$ NSA at representative wavelengths of 550 nm and 705 nm are provided in Figs. 5(a) and (b). The absorption at a specific wavelength is calculated by carrying out a volume integral of the

absorption density (p_{abs}) corresponding to the absorbed power per unit volume ($P_{abs} = \frac{1}{2}\omega\varepsilon''|E|^2$ where ω is the angular frequency, ε'' is the imaginary part of the permittivity of the material, and $|E|^2$ is the electric field intensity) normalized by the light source, which can be expressed as:

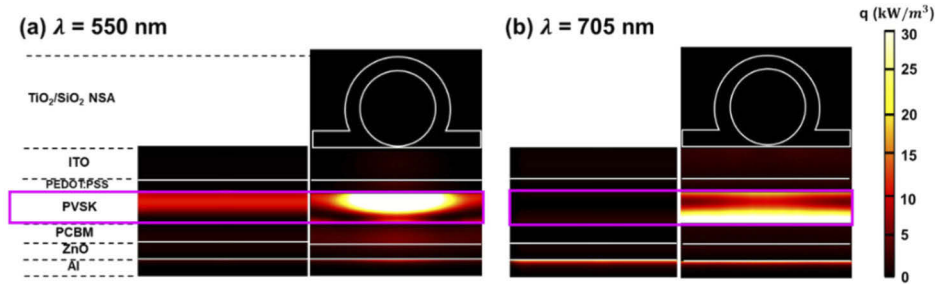$$Absorption(\lambda) = \int p_{abs}(\lambda)dV \qquad (2)$$

Fig. 5. Absorption distributions into the PSC structures without (left) and with (right) TiO$_2$/SiO$_2$ NSA at (a) 550 nm and (b) 705 nm.

As can be seen from Fig. 5(a), the absorption in the thin PVSK photoactive layer is significantly enhanced with the help of the TiO$_2$/SiO$_2$ NSA at 550 nm, whereas the absorption in the other layers is trivial compared to the photoactive layer.

Since the forward scattering dominantly occurs in all directions at 550 nm, the TiO$_2$/SiO$_2$ NSA functions as a lens to highly focus incident light into the transparent ITO layer and then defocus light in the ultrathin PVSK photoactive layer. This can increase the optical path length in the photoactive layer yielding the light absorption enhancement. Since the extinction coefficient of the PVSK material decreases with increasing the wavelength (see Fig. 2(e)), the absorption in the photoactive layer at 705 nm is highly limited as shown in the left of Fig. 5(b). Such reduced absorptions in the longer wavelength region can be remarkably improved by the excellent LT effect of the TiO$_2$/SiO$_2$ NSA that supports Mie resonances yielding the better light coupling into the photoactive layer. This is ascribed to the strong far-field forward-scattering arising from high optical density of states, leading to the increase in the optical path length in the photoactive layer by redirecting the normally incident light along more horizontal directions. In addition to the aforementioned strong forward-scattering of light from the resonant Mie scattering, the AR effect due to a better index matching and a graded refractive index profile contributes to the absorption enhancements in the photoactive layer. It is noteworthy that the scattering for the LT effect may be further improved by finding an optimized shape or a refractive index combination of the TiO$_2$/SiO$_2$ NSA, which is beyond the scope of this work. It is also worth mentioning that the total (direct + diffuse) transmission obtained from the planar PSC structure with the TiO$_2$/SiO$_2$ NSA is overall lower than that attained from the planar PSC structure without the TiO$_2$/SiO$_2$ NSA, when illuminated from the bottom portion of the cell. This suggests that the light reflected from the back Al contact is not guided forwardly to escape outside the cell through the TiO$_2$/SiO$_2$ NSA, which could be attributed to the fact that the TiO$_2$/SiO$_2$ NSA was optimally designed for the light illumination from the top side of the PSC structure. The conformal SiO$_2$ layer can function as the efficient anti-reflection (AR) coating when illuminated from the air as the refractive index of SiO$_2$ ($n = 1.47$) is close to the optimal index for the AR coating ($\sqrt{n_{air}n_{TiO2}} = \sqrt{1 \times 2.40} \approx 1.55$), but cannot function as the efficient AR coating when illuminated from the bottom side of the cell due to the index mismatch ($\sqrt{n_{ITO}n_{TiO2}} = \sqrt{1.81 \times 2.40} \approx 2.08$).

Figures 6(a) and (b) exhibit spectra of the scattering cross-section (σ_{sca}) and the corresponding multipole decompositions calculated for the TiO$_2$ nanosphere with D of 240 nm in air and for a core-shell nanosphere structure consisting of an inner TiO$_2$ nanosphere ($D = 220$ nm) coated with

the thin SiO$_2$ layer ($t = 75$ nm), respectively. Since more light is scattered in the forward direction with increasing the size of the nanoparticle according to the Mie theory, adding a conformal dielectric layer to the original nanoparticle basically increases the size of the overall nanoparticle thus allowing more forward light scattering to occurs. In addition, the conformal coating layer refracts incident light, thus resulting in a large scattering cross-section as compared to the single nanoparticle as depicted in inset images in Figs. 6(a) and (b). Peaks of the electric dipole (ED), magnetic dipole (MD), electric quadrupole (EQ), and magnetic quadrupole (MQ) shift toward the longer wavelength region with increasing the diameter and the gap of the nanoparticles. It is well-known that the ED resonance is broadened and shifted toward the longer wavelength region while the shift in the MD resonance is trivial but the broadening still occurs when the spherical particles are surrounded by any materials as compared to the particles in vacuum according to the Mie theory. The strategy here is to exploit a relative sensitivity of the electric resonant modes with respect to the refractive index of the surrounding medium as compared to the magnetic resonances. The ED resonance shifts from 510 nm to 640 nm and the EQ resonance moves from 395 nm to 440 nm, whereas the position of the MD resonance is shifted from 605 nm to 640 nm and the MQ resonance shifts from 450 nm to 460 nm, after applying the conformal SiO$_2$ coating to the TiO$_2$ nanosphere. The ED (EQ) overlaps with the MD (MQ) leading to the enhanced scattering as revealed in Figs. 6(a) and (b).
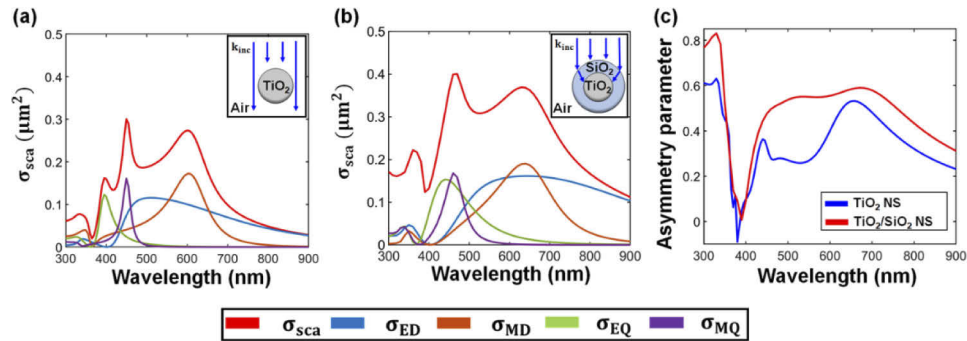

Fig. 6. Scattering cross-sections and the corresponding multipoles' contributions for (a) the TiO$_2$ nanosphere with D of 240 nm in air and (b) the TiO$_2$/SiO$_2$ nanosphere with D of 220 nm and t of 75 nm in air. (c) Asymmetry parameters calculated for the TiO$_2$ nanosphere (blue) and TiO$_2$/SiO$_2$ nanosphere (red).

Since the EQ resonance approaches the MQ resonance with the conformal 75 nm-thick SiO$_2$ coating, a pronounced and broadened peak at 470 nm occurs in σ_{sca}, which significantly enhance the light scattering in the forward direction and thus the absorption in the PVSK photoactive layer as depicted in Fig. 4(b).

The strong scattering property at 640 nm is due to the combined ED and MD resonances, which is responsible for enhancing the absorption in the photoactive layer at the longer wavelength region. By choosing a proper thickness of the conformal SiO$_2$ coating, σ_{sca} of the TiO$_2$ nanosphere is greatly enhanced over a broad wavelength range, which are highly beneficial for the efficient LT effect by the prominent light scattering property. The scattering cross-sections for the ED (σ_{ED}), MD (σ_{MD}), EQ (σ_{EQ}), and MQ (σ_{MQ}) are calculated by using the following equations:

$$\sigma_{ED} = \frac{k_0^4}{6\pi\varepsilon_0^2 E_0^2} \sum_\alpha |p_\alpha|^2 \tag{3}$$

$$\sigma_{MD} = \frac{k_0^4 \varepsilon \mu_0}{6\pi\varepsilon_0 E_0^2} \sum_\alpha |m_\alpha|^2 \tag{4}$$

$$\sigma_{EQ} = \frac{k_0^6 \varepsilon}{720\pi\ \varepsilon_0^2 E_0^2} \sum\nolimits_{\alpha\beta} |Q_{\alpha\beta}|^2 \tag{5}$$

$$\sigma_{MQ} = \frac{k_0^6 \varepsilon^2 \mu_0}{80\pi\varepsilon_0 E_0^2} \sum\nolimits_{\alpha\beta} |M_{\alpha\beta}|^2 \tag{6}$$

where $p_\alpha = \int_V \{ j_0(kr') P_\alpha(r') + \frac{3k^2 j_2(kr')}{2(kr')^2} \left[(\overrightarrow{r'}, \overrightarrow{P(r')}) r'_\alpha - \frac{1}{3} r'^2 P_\alpha \right] \} dV$, $m_\alpha = \frac{3\omega}{2i} \int_V \{ \frac{j_1(kr')}{kr'} [\overrightarrow{r'}$ $\times \overrightarrow{P(r')}], \hat{\alpha} \} dV$, $Q_{\alpha\beta} = 3 \int_V \{ \frac{j_1(kr')}{kr'} [3(r'_\alpha P_\beta(r') + P_\alpha(r') r'_\beta) - 2(\overrightarrow{r'}, \overrightarrow{P(r')}), \delta_{\alpha\beta}] + \frac{2k^2 j_3(kr')}{(kr')^3}$ $[5r'_\alpha r'_\beta (\overrightarrow{r'}, \overrightarrow{P(r')}) - (r'_\alpha P_\beta(r') + P_\alpha(r') r'_\beta) r'^2 - r'^2 (\overrightarrow{r'}, \overrightarrow{P(r')}) \delta_{\alpha\beta}] \} dV$, and $M_{\alpha\beta} = \frac{15\omega}{i} \int_V \{ \frac{j_2(kr')}{(kr')^2}$ $[r'_\alpha (\overrightarrow{r'} \times \overrightarrow{P(r')}), \hat{\beta} + r'_\beta (\overrightarrow{r'} \times \overrightarrow{P(r')}), \hat{\alpha}] \} dV$ represent the ED, MD, EQ, and MQ momenta, respectively, α and β denote x, y, z, $j_l(kr')$ is the lth order spherical Bessel function, ε is a permittivity of surrounding medium, k is a wave number in the surrounding medium, k_0 is a wave number in vacuum, ω is an angular frequency of incident light, V and S represent a volume and a surface of a scatterer particle, $\overrightarrow{P(r')}$ is the polarization induced by an external electromagnetic field and P_α is a polarization value of α direction [44,45]. It is worth noting that geometry cross-sections for the TiO$_2$ nanosphere and the TiO$_2$/SiO$_2$ nanosphere are 0.045 μm^2 and 0.108 μm^2, respectively. We also investigate the asymmetry parameter ($g = \int_S I_{sca} \cos\theta\ dS / \int_S I_{sca}\ dS$, where I_{sca} is the irradiance of scattered light by scatterer function of solid angle and $\cos\theta$ represents the angle between incident light direction and scattered light direction), which is used to quantify the directivity of the light scattering, thus implying that the direction of the scattered power [46]. Figure 6(c) presents the spectra of the asymmetry parameter (g) calculated for the TiO$_2$ nanosphere (blue) and TiO$_2$/SiO$_2$ nanosphere (red), exhibiting that high g values greater than 0.55 are achieved from 450 nm to 700 nm with the TiO$_2$/SiO$_2$ nanosphere LT structure, which suggests that most of the incident energy is scattered in the forward direction. As is seen from the figure, g obtained from the TiO$_2$/SiO$_2$ nanosphere is higher than g attained from the TiO$_2$ nanosphere over the entire visible solar spectrum, which validates the high and broad scattering cross-section achieved from the TiO$_2$/SiO$_2$ nanosphere as observed in Figs. 6(a) and (b). It is worth mentioning that the total σ_{sca} calculated by using $\int_S I_{sca}\ dS / I_{inc}$ where I_{inc} is the irradiance of incident light agrees well with the sum of the multipoles. The multipole resonant contributions of the different core-shell nanoparticle structures were investigated in previous works [47,48].

Figures 7(a) and (b) describe far-field radiation patterns of the TiO$_2$ nanosphere and the TiO$_2$/SiO$_2$ nanosphere at 550 nm and 705 nm, respectively, revealing that the relative far-field irradiance of the TiO$_2$/SiO$_2$ nanosphere is about twice higher than that of the TiO$_2$ nanosphere with a greater scattering angle. Such an increased angle of the light scattering in the forward direction provides the noticeable optical path length enhancement in the PVSK photoactive layer, thereby contributing to the generation of the higher J_{sc}. The radiation patterns are resulting from the optical interference effect between the fields generated by the dipole and quadrupole multipolar moments, which can determine the direction of the light scattering.

In Figs. 8(a) and (b), incident-angle-dependent J_{sc} values generated by the planar PSC (black) and the PSCs with TiO$_2$ NSA (blue) and with TiO$_2$/SiO$_2$ NSA (red) for TE and TM polarizations are depicted. The J_{sc} for the three cases decreases with increasing the incident angles for TE polarization, presenting that the J_{sc} of 14.5 mA/cm^2 obtained from the PSC structure with the integration of the TiO$_2$/SiO$_2$ NSA at 70° is still higher than that of 14.2 mA/cm^2 attained from the flat PSC at normal incidence. It is noticed that a small J_{sc} reduction for angles varying between 0° and 70° is observed after incorporating the TiO$_2$/SiO$_2$ NSA (77.5%) as compared to the flat PSC (56.3%) for TE polarization. For TM polarization, the J_{sc} generated by the PSC integrated with the TiO$_2$/SiO$_2$ NSA LT structure is higher than that obtained from the flat PSC structure for the incident angles up to 54°.
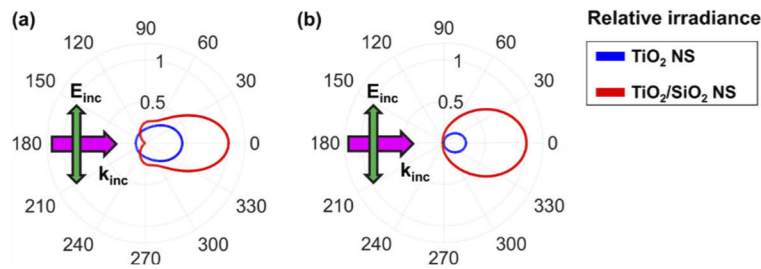
Fig. 7. Radiation patterns of the TiO_2 nanosphere with D of 240 nm (blue) and the TiO_2/SiO_2 nanosphere with D of 220 nm and t of 75 nm (red) calculated at (a) 550 nm and (b) 705 nm.
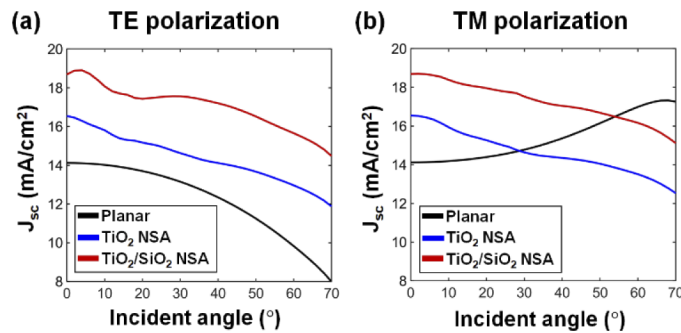

Fig. 8. Calculated J_{sc} values as a function of incident angles for (a) TE and (b) TM polarizations.

3. Conclusion

In summary, we have demonstrated the absorption enhancement in the ultrathin PSC structure by the incorporation of the TiO_2/SiO_2 NSA LT structure. Strong scattering combined with the AR coating effect of the TiO_2/SiO_2 NSA with the optimized featured parameters allows σ_{sca} to be enhanced and broadened so that incident light can be significantly absorbed in the ultrathin PVSK photoactive layer over a broad spectral range, thereby achieving the J_{sc} of 18.7 mA/cm^2. The scattering cross-sections, the spectral multipole resonances, the asymmetry parameters, and the far-field radiation patterns are investigated displaying the enhanced forward scattering with the reduced backward scattering over a broad range of the wavelengths, which is responsible for the significant improvement of the absorption in the ultrathin PVSK layer. The approach described in this work could potentially extend the range of possible applications.

Disclosures. The authors declare that there are no conflicts of interest related to this article.

Data availability. Simulation data underlying the results presented in this paper may be obtained from the authors upon reasonable request.

References

1. M. A. Green, A. Ho-Baillie, and H. J. Snaith, "The emergence of perovskite solar cells," Nat. Photonics **8**(7), 506–514 (2014).
2. J. Y. Kim, J.-W. Lee, H. S. Jung, H. Shin, and N.-G. Park, "High-Efficiency Perovskite Solar Cells," Chem. Rev. **120**(15), 7867–7918 (2020).

3. G. E. Eperon, M. T. Hörantner, and H. J. Snaith, "Metal halide perovskite tandem and multiple-junction photovoltaics," Nat. Rev. Chem. **1**(12), 0095 (2017).

4. S. D. Stranks and H. J. Snaith, "Metal-halide perovskites for photovoltaic and light-emitting devices," Nat. Nanotech. **10**(5), 391–402 (2015).

5. G. Pacchioni, "Highly efficient perovskite LEDs," Nat. Rev. Mater. **6**(2), 108 (2021).

6. Q. Van Le, H. W. Jang, and S. Y. Kim, "Recent Advances toward High-Efficiency Halide Perovskite Light-Emitting Diodes: Review and Perspective," Small Methods **2**(10), 1700419 (2018).

7. H. Wang and D. H. Kim, "Perovskite-based photodetectors: materials and devices," Chem. Soc. Rev. **46**(17), 5204–5236 (2017).

8. M. Ahmadi, T. Wu, and B. Hu, "A Review on Organic–Inorganic Halide Perovskite Photodetectors: Device Engineering and Fundamental Physics," Adv. Mater. **29**(41), 1605242 (2017).

9. Q. Dong, Y. Fang, Y. Shao, P. Mulligan, J. Qiu, L. Cao, and J. Huang, "Electron-hole diffusion lengths > 175 μm in solution-grown $CH_3NH_3PbI_3$ single crystals," Science **347**(6225), 967–970 (2015).

10. D. Shi, V. Adinolfi, R. Comin, M. Yuan, E. Alarousu, A. Buin, Y. Chen, ven-names>S. Hoogland, A. Rothenberger, K. Katsiev, Y. Losovyj, X. Zhang, P. A. Dowben, O. F. Mohammed, E. H. Sargent, and O. M. Bakr, "Low trap-state density and long carrier diffusion in organolead trihalide perovskite single crystals," Science **347**(6221), 519–522 (2015).

11. S. D. Stranks, G. E. Eperon, G. Grancini, C. Menelaou, M. J. P. Alcocer, T. Leijtens, L. M. Herz, A. Petrozza, and H. J. Snaith, "Electron-Hole Diffusion Lengths Exceeding 1 Micrometer in an Organometal Trihalide Perovskite Absorber," Science **342**(6156), 341–344 (2013).

12. C. Wehrenfennig, G. E. Eperon, M. B. Johnston, H. J. Snaith, and L. M. Herz, "High Charge Carrier Mobilities and Lifetimes in Organolead Trihalide Perovskites," Adv. Mater. **26**(10), 1584–1589 (2014).

13. J. H. Noh, S. H. Im, J. H. Heo, T. N. Mandal, and S. I. Seok, "Chemical Management for Colorful, Efficient, and Stable Inorganic–Organic Hybrid Nanostructured Solar Cells," Nano Lett. **13**(4), 1764–1769 (2013).

14. A. Kojima, K. Teshima, Y. Shirai, and T. Miyasaka, "Organometal halide perovskites as visible-light sensitizers for photovoltaic cells," J. Am. Chem. Soc. **131**(17), 6050–6051 (2009).

15. J. Jeong, M. Kim, J. Seo, H. Lu, P. Ahlawat, A. Mishra, Y. Yang, M. A. Hope, F. T. Eickemeyer, M. Kim, Y. J. Yoon, I. W. Choi, B. P. Darwich, S. J. Choi, Y. Jo, J. H. Lee, B. Walker, S. M. Zakeeruddin, L. Emsley, U. Rothlisberger, A. Hagfeldt, D. S. Kim, M. Grätzel, and J. Y. Kim, "Pseudo-halide anion engineering for α-FAPbI3 perovskite solar cells," Nature **592**(7854), 381–385 (2021).

16. B. Shi, L. Duan, Y. Zhao, J. Luo, and X. Zhang, "Semitransparent Perovskite Solar Cells: From Materials and Devices to Applications," Adv. Mater. **32**(3), 1806474 (2020).

17. K.-T. Lee, L. J. Guo, and H. J. Park, "Neutral- and Multi-Colored Semitransparent Perovskite Solar Cells," Molecules **21**(4), 475 (2016).

18. Q. Wali, N. K. Elumalai, Y. Iqbal, A. Uddin, and R. Jose, "Tandem perovskite solar cells," Renew. Sustainable Energy Rev. **84**, 89–110 (2018).

19. H. Li and W. Zhang, "Perovskite Tandem Solar Cells: From Fundamentals to Commercial Deployment," Chem. Rev. **120**(18), 9835–9950 (2020).

20. M. Jošt, L. Kegelmann, L. Korte, and S. Albrecht, "Monolithic Perovskite Tandem Solar Cells: A Review of the Present Status and Advanced Characterization Methods Toward 30% Efficiency," Adv. Energy Mater. **10**(26), 1904102 (2020).

21. Y. Bai, X. Meng, and S. Yang, "Interface Engineering for Highly Efficient and Stable Planar p-i-n Perovskite Solar Cells," Adv. Energy Mater. **8**(5), 1701883 (2018).

22. M. B. Schubert and J. H. Werner, "Flexible solar cells for clothing," Mater. Today **9**(6), 42–50 (2006).

23. S. Pan, Z. Yang, P. Chen, J. Deng, H. Li, and H. Peng, "Wearable Solar Cells by Stacking Textile Electrodes," Angew. Chem. Int. Ed. **53**(24), 6110–6114 (2014).

24. H. Jinno, K. Fukuda, X. Xu, S. Park, Y. Suzuki, M. Koizumi, T. Yokota, I. Osaka, K. Takimiya, and T. Someya, "Stretchable and waterproof elastomer-coated organic photovoltaics for washable electronic textile applications," Nat Energy **2**, 780–785 (2017).

25. M. Kaltenbrunner, G. Adam, E. D. Głowacki, M. Drack, R. Schwödiauer, L. Leonat, D. H. Apaydin, H. Groiss, M. C. Scharber, M. S. White, N. S. Sariciftci, and S. Bauer, "Flexible high power-per-weight perovskite solar cells with chromium oxide–metal contacts for improved stability in air," Nat. Mater. **14**(10), 1032–1039 (2015).

26. H. Jinno, T. Yokota, M. Koizumi, W. Yukita, M. Saito, I. Osaka, K. Fukuda, and T. Someya, "Self-powered ultraflexible photonic skin for continuous bio-signal detection via air-operation-stable polymer light-emitting diodes," Nat. Commun. **12**(1), 2234 (2021).

27. A. R. Pascoe, S. Meyer, W. Huang, W. Li, I. Benesperi, N. W. Duffy, L. Spiccia, U. Bach, and Y.-B. Cheng, "Enhancing the Optoelectronic Performance of Perovskite Solar Cells via a Textured CH3NH3PbI3 Morphology," Adv. Funct. Mater. **26**(8), 1278–1285 (2016).

28. L. Zheng, Y. Ma, S. Chu, S. Wang, B. Qu, L. Xiao, Z. Chen, Q. Gong, Z. Wu, and X. Hou, "Improved light absorption and charge transport for perovskite solar cells with rough interfaces by sequential deposition," Nanoscale **6**(14), 8171–8176 (2014).

29. M. Jošt, S. Albrecht, L. Kegelmann, C. M. Wolff, F. Lang, B. Lipovšek, J. Krč, L. Korte, D. Neher, B. Rech, and M. Topič, "Efficient Light Management by Textured Nanoimprinted Layers for Perovskite Solar Cells," ACS Photonics **4**(5), 1232–1239 (2017).

30. A. Tooghi, D. Fathi, and M. Eskandari, "Numerical study of a highly efficient light trapping nanostructure of perovskite solar cell on a textured silicon substrate," Sci. Rep. **10**(1), 18699 (2020).

31. J. Q. Xi, M. F. Schubert, J. K. Kim, E. F. Schubert, M. Chen, S.-Y. Lin, W. Liu, and J. A. Smart, "Optical thin-film materials with low refractive index for broadband elimination of Fresnel reflection," Nat. Photonics **1**(3), 176–179 (2007).

32. C. Battaglia, J. Escarré, K. Söderström, M. Charrière, M. Despeisse, F.-J. Haug, and C. Ballif, "Nanomoulding of transparent zinc oxide electrodes for efficient light trapping in solar cells," Nat. Photonics **5**(9), 535–538 (2011).

33. Q. Luo, C. Zhang, X. Deng, H. Zhu, Z. Li, Z. Wang, X. Chen, and S. Huang, "Plasmonic Effects of Metallic Nanoparticles on Enhancing Performance of Perovskite Solar Cells," ACS Appl. Mater. Interfaces **9**(40), 34821–34832 (2017).

34. R. T. Ginting, S. Kaur, D.-K. Lim, J.-M. Kim, J. H. Lee, S. H. Lee, and J.-W. Kang, "Plasmonic Effect of Gold Nanostars in Highly Efficient Organic and Perovskite Solar Cells," ACS Appl. Mater. Interfaces **9**(41), 36111–36118 (2017).

35. A. A. Mohsen, M. Zahran, S. E. D. Habib, and N. K. Allam, "Refractory plasmonics enabling 20% efficient lead-free perovskite solar cells," Sci. Rep. **10**(1), 6732 (2020).

36. M. Long, Z. Chen, T. Zhang, Y. Xiao, X. Zeng, J. Chen, K. Yan, and J. Xu, "Ultrathin efficient perovskite solar cells employing a periodic structure of a composite hole conductor for elevated plasmonic light harvesting and hole collection," Nanoscale **8**(12), 6290–6299 (2016).

37. Y. Xiao, C. Wang, K. K. Kondamareddy, N. Cheng, P. Liu, Y. Qiu, F. Qi, S. Kong, W. Liu, and X.-Z. Zhao, "Efficient Electron Transport Scaffold Made up of Submicron TiO2 Spheres for High-Performance Hole-Transport Material Free Perovskite Solar Cells," ACS Appl. Energy Mater. **1**, 5453–5462 (2018).

38. A. Peer, R. Biswas, J.-M. Park, R. Shinar, and J. Shinar, "Light management in perovskite solar cells and organic LEDs with microlens arrays," Opt. Express **25**(9), 10704–10709 (2017).

39. D.-L. Wang, H.-J. Cui, G.-J. Hou, Z.-G. Zhu, Q.-B. Yan, and G. Su, "Highly efficient light management for perovskite solar cells," Sci. Rep. **6**(1), 18922 (2016).

40. H. A. Atwater and A. Polman, "Plasmonics for improved photovoltaic devices," Nat. Mater. **9**(3), 205–213 (2010).

41. A. Tooghi, D. Fathi, and M. Eskandari, "High-performance perovskite solar cell using photonic–plasmonic nanostructure," Sci. Rep. **10**(1), 11248 (2020).

42. M. Fukuda, K. T. Lee, J. Y. Lee, and L. J. Guo, "Optical Simulation of Periodic Surface Texturing on Ultrathin Amorphous Silicon Solar Cells," IEEE J. Photovoltaics **4**(6), 1337–1342 (2014).

43. C. Zuo and L. Ding, "Modified PEDOT Layer Makes a 1.52 V Voc for Perovskite/PCBM Solar Cells," Adv. Energy Mater. **7**(2), 1601193 (2017).

44. A. B. Evlyukhin and B. N. Chichkov, "Multipole decompositions for directional light scattering," Phys. Rev. B **100**(12), 125415 (2019).

45. R. Alaee, C. Rockstuhl, and I. Fernandez-Corbaton, "An electromagnetic multipole expansion beyond the long-wavelength approximation," Opt. Commun. **407**, 17–21 (2018).

46. P. D. Terekhov, H. K. Shamkhi, E. A. Gurvitz, K. V. Baryshnikova, A. B. Evlyukhin, A. S. Shalin, and A. Karabchevsky, "Broadband forward scattering from dielectric cubic nanoantenna in lossless media," Opt. Express **27**(8), 10924–10935 (2019).

47. J. Zhou, A. Panday, Y. Xu, X. Chen, L. Chen, C. Ji, and L. Jay Guo, "Visualizing Mie Resonances in Low-Index Dielectric Nanoparticles," Phys. Rev. Lett. **120**(25), 253902 (2018).

48. R. Li, X. Zhou, M. Panmai, J. Xiang, H. Liu, M. Ouyang, H. Fan, Q. Dai, and Z. Wei, "Broadband zero backward scattering by all-dielectric core-shell nanoparticles," Opt. Express **26**(22), 28891–28901 (2018).